# We are IntechOpen,
## the world's leading publisher of Open Access books
## Built by scientists, for scientists

**4,800**
Open access books available

**122,000**
International authors and editors

**135M**
Downloads

**154**
Countries delivered to

Our authors are among the

**TOP 1%**
most cited scientists

**12.2%**
Contributors from top 500 universities

CLARIVATE ANALYTICS
**BOOK CITATION INDEX**
INDEXED

**WEB OF SCIENCE**™

Selection of our books indexed in the Book Citation Index
in Web of Science™ Core Collection (BKCI)

## Interested in publishing with us?
## Contact book.department@intechopen.com

# Field Emission from Graphene Nanosheets

Takahiro Matsumoto[1,4], Tomonori Nakamura[3,5],
Yoichiro Neo[3], Hidenori Mimura[3] and Makoto Tomita[6]
[1]*Research and Development Center, Stanley Electric Corporation*
[2]*Center for Quantum Science and Technology, Osaka University*
[3]*Research Institute of Electronics, Shizuoka University*
[4]*National Institute of Advanced Industrial Science and Technology*
[5]*Research Laboratory, Onizuka Glass Corporation*
[6]*Department of Physics, Shizuoka University*
*Japan*

## 1. Introduction

The 2D graphene sheet structure is promising for field emission of electrons, because the carrier mobility and electron mass were reported to have exceptionally large and small values, respectively, due to the quantum relativistic effect (Novoselov et al., 2005; Zhang et al., 2005; Geim & Novoselov, 2007).

In this chapter, we overview the superior aspects of field emitter by using a multi layered graphene nanosheet structure (GNS) and give quantitative description of the physics of electron field emission from this GNS. Firstly (section 2&3), we briefly overview the fabrication method, structure characterization, and field emission current characteristics of GNS. Secondly (section 4), we describe the correlation between the emission current fluctuation and molecular adsorption, because the emission current is affected both by the adsorption and desorption of molecules and by the temperature of the emission sites onto the graphene sheet. However, there is no quantitative discussion to describe the adsorption process of field emission. Therefore, we construct a stochastic model based on the physisorption of atoms and/or molecules onto the emission sites, which can be applied to other types of field emitters. Here macroscale statistical discussion is shown to give insights for microscale emission mechanism. Thirdly (section 5), we will proceed atomic level studies by using a field emission microscopy, which gives fruitful information on the microscopic origin of the emission from graphene. Symmetrical emission patterns such as two-fold, four-fold, and ring patterns were observed. These symmetrical patterns are experimentally correlated with the excitation mode of $\pi$ conjugated bonds and are theoretically explained from the excited modes of six membered ring in the graphene sheet. These results and theoretical analyses give the solution to the mystery of FEM patterns obtained by other types of carbon materials such as phthalocyanine argued for more than 60 years. After the clarification of the fundamental aspects of GNS, we overview the application aspects of the GNS field emitter (section 6). The high performance of the field emitter is presented by the demonstration of a time resolved x-ray radiography system and a field emission scanning

electron microscope (FE-SEM) system. We will also present our recent progress in miniature sized x-ray tubes with GNS field emitter. The tube has both the lifetime more than 10,000 hours and the stability better than 1 %; therefore, we believe GNS is best suited for field emitters. We will put the x-ray tube into practical use in coming years. Finally (section 7), we will give our future prospects for the GNS field emitter.

## 2. Fabrication and nanostructure characterization

The GNS field emitters are fabricated by hydrogen plasma etching of a carbon rod in a microwave (a frequency of 2.45 GHz) plasma chemical vapor deposition equipment as shown in Fig. 1. Typical etching condition is as follows; a microwave power of 800 W, a gas pressure of 1.3 kPa, a $H_2$ gas flow rate of 80 sccm, a substrate temperature of 600 ˚C, a substrate bias of -200 V, and an etching time of 30 min (Matsumoto & Mimura, 2004; Matsumoto & Mimura, 2005).
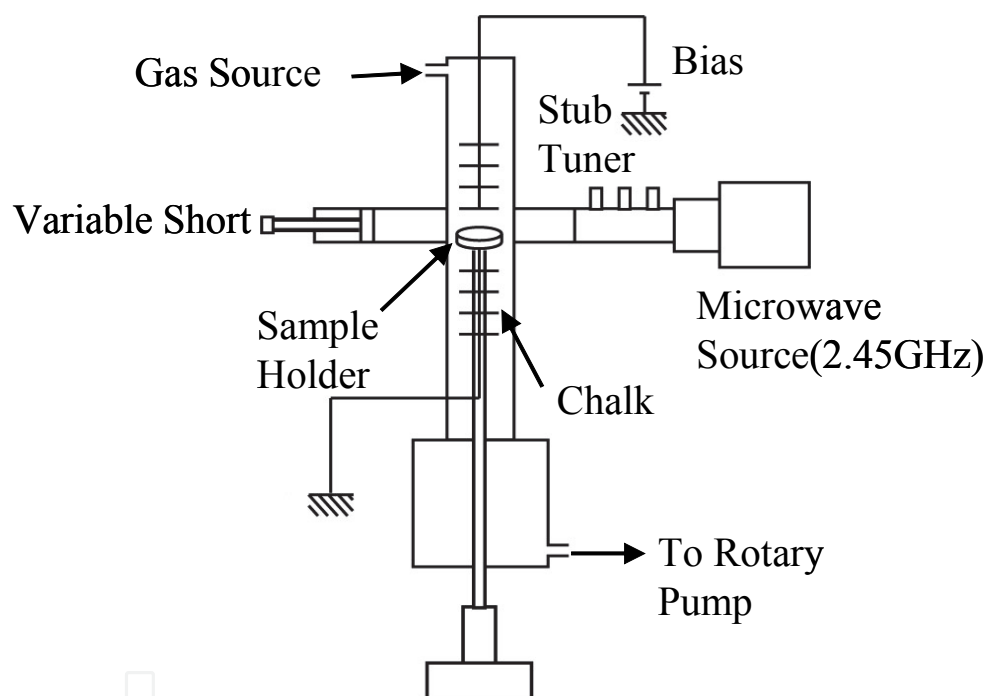


Fig. 1. Schematic of a microwave plasma CVD equipment for hydrogen plasma etching. (Reprinted with permission, Matsumoto & Mimura 2005, American Institute of Physics.)

A carbon rod with a diameter of 0.5 mm φ is mechanically sharpened at one end to less than a 10 μm φ diameter as shown in Fig. 2 (a) before the plasma etching and then nanoneedles are fabricated on the tip by the hydrogen plasma etching. An SEM image of a carbon rod after hydrogen plasma etching is shown in Fig. 2 (b). A lot of nanoneedles are fabricated on the spearhead region of the graphite rod. A transmission electron microscope (TEM) image of one nanoneedle is shown in Fig. 2 (c). Typical aspect ratio of the nanoneedle is on the order of 1000. The radius of curvature in the top region of the needle is less than 5 nm. This small radius and the high aspect ratio make it suitable for a field electron emission cathode. A high resolution TEM image of the nanoneedle is shown in Fig. 2 (d). A lattice fringe pattern is clearly observed from the bottom to the top of the needle as shown in Fig. 2 (d). Based on the lattice fringe and diffraction patterns (c axis) shown in Fig. 2 (d), the top region

of the nanoneedle consists of a two-dimensional graphene sheet with an interplanar spacing of 0.36 nm (Matsumoto et al., 2007; Matsumoto et al., 2008). This value is larger than that of the hexagonal graphite structure (0.34 nm), which indicates that the c-axis lattice is relaxed. Another diffraction pattern (a axis) whose direction is orthogonal to the interplanar direction is observed. Based on the distance of a-axis diffraction patterns, we can determine the atomic level of spacing, and this is 0.21 nm. This value corresponds to (010) plane spacing of the six membered ring in the graphene sheet. Therefore, the interaction between the graphene sheets is weakened due to the expansion of the interplanar lattice spacing, thus the GNS possesses the two dimensional (2D) aspects compared to the three dimensional graphite structure. As well as the weakened interplaner interaction, the 2D graphene sheet structure with the lattice fringes from the bottom to the top direction is promising for field emission, because the carrier mobility and electron mass are shown to have exceptionally large ($\mu$= 15000 $cm^2$ $V^{-1}$ $s^{-1}$) and small (0.007$m_e$, $m_e$: free electron mass) values in this 2D system (Novoselov et al., 2005; Geim & Novoselov, 2007).
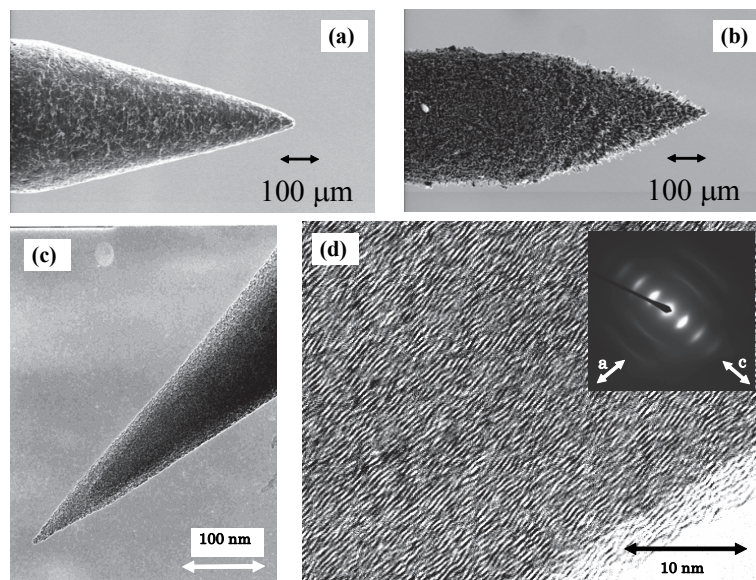


Fig. 2. SEM Image of a carbon rod: (a) before hydrogen plasma etching and (b) after hydrogen plasma etching. (c) TEM image of a single GNS emitter. (d) High-resolution TEM image. Inset shows the selected area electron diffraction pattern of a single GNS emitter. (Reprinted with permission, Matsumoto et al. 2007, American Institute of Physics.)

## 3. Field emission characteristics

Fowler and Nordheim (FN) first derived a semiclassical theory of field emission currents from cold metals in 1928 (Fowler & Nordheim, 1928). In this theory, the system is simplified as a one-dimensional structure along the direction of the external field. The emission tip is modeled as a semi-infinite quantum well. By employing the Wentzel-Kramers-Brillouin approximation, following FN plot is given.

$$ln\ (I/V^2) \propto -1/V \tag{1}$$

where I is in amperes per square centimeter of emitting surface and V is the applied voltage.
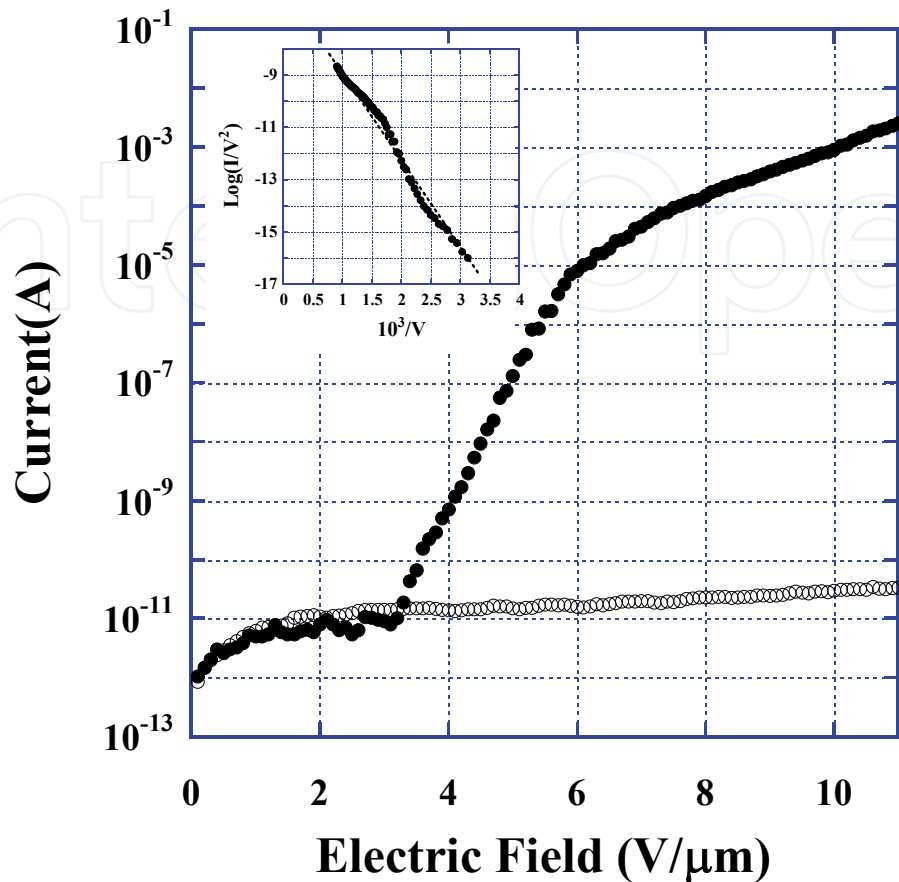
Fig. 3. Current-voltage characteristics for a mechanically sharpened carbon rod (open circles) and a GNS cathode (solid circles). Inset shows the Fowler-Nordheim plots (ln(I/V²) vs 1/V) for the I-V characteristics of the GNS cathode. (Reprinted with permission, Matsumoto et al. 2007, American Institute of Physics.)

The above FN theory should not be applied to nanometer sized emitters such as GNS and CNT because the geometrical size of the tip is comparable to the electron wavelength. Much sophisticated emission theory is developed by several authors (He et al., 1991; Liang & Chen, 2008; Forbes, 2001), and these theories will explain the difference between the straight line obtained by the simple FN plot and the experimentally obtained slightly curved feature (dotted line) in the inset of Fig. 3. For the precise fitting by using these sophisticated theories, it is necessary to determine physical values such as a shape and a size as well as the electronic properties; e.g. the defect density and work function of the tip. However, as shown in Fig. 2, it is difficult to determine these values for our tip. Therefore, here we estimate the field emission characteristics by using the FN plots.

Figure 3 shows typical logarithmic current-voltage (I-V) characteristic of the GNS field emitter. The figure also shows I-V characteristic of a sharpened graphite rod without nanostructure. The currents were collected on a 3 mm ϕ diameter aluminum anode, which was located at 100 μm in front of the cathode. The measurements were carried out in a

vacuum chamber with a residual pressure of 1 x 10<sup>-6</sup> Pa. The mechanically sharpened graphite rod without nanostructure showed little field emission current (open circles), while the GNS emitter starts to emit electrons at an average electric field of about 3 V/μm and the emission current exceeds 2 mA at an applied electric field of 11 V/μm (solid circles). The FN plot of the emission current from the GNS emitter is shown in the inset of Fig. 3. Linear dependence of the Fowler-Nordheim plot suggests that the electron emission is dominated by the Fowler-Nordheim tunneling process as described in Eq. (1).

## 4. Emission current fluctuation and stochastic birth and death model

The electronic properties of nanomaterials are very sensitive to the adsorption of molecules (Kong et al., 2000; Zhao et al., 2002; Grujicic et al., 2003; Andzelm et al., 2006). This characteristic is clearly observed when measuring field emission-current fluctuations of carbon nanostructures, where the emission current stability is easily lost under high residual pressure and the stability is obtained by thermally desorbing adsorbed molecules onto the emission sites. This phenomenon can be explained as the adsorption and desorption of molecules onto emission sites of carbon nanostructures with the molecules adsorbing onto the nanostructures affecting the electronic properties, such as charge transfer and tunneling probability (Dyke & Dolan, 1956; Gadzuk & Plummer, 1973).

In this section, we show a model in which the field emission current fluctuation originates from the adsorption and desorption of molecules onto the emission sites, which is well described using a stochastic birth and death model (Feller, 1957). The emission current fluctuation was analyzed as a cathode temperature using differential equations obtained from the model. We derive the Poisson distribution for the deviation of the fluctuating emission current and finally, we show the method of the determination of physisorption energy of various molecules using the field emission current fluctuation.

Figure 4 shows the fluctuating emission current distribution measured in a 10<sup>-4</sup> Pa $H_2$ atmosphere at different temperatures. The current intensity distribution at 300 K shown in Fig. 4 (solid circles) gives the current fluctuation deviation, $\Delta I / I_p = 0.31$, where $\Delta I$ is the full width at half maximum (FWHM) of the fluctuation and $I_p$ is the peak value of the current. The deviation can be reduced by heating the cathode: $\Delta I / I_p = 0.21$ at 700 K (solid triangles), and $\Delta I / I_p = 0.16$ at 925 K (solid squares). This reduction in the deviation suggests that heating is an effective way to stabilize the field emission current. Along with the reduction of the deviation, the peak of the current distribution shifts to the lower current side with increasing cathode temperature. Both the reduction of the deviation and the lower peak shift of the current distribution can be interpreted qualitatively as the adsorption and desorption of atoms or ions on or off surface of the emission sites (Hosoki et al., 1979; Yamamoto et al., 1979).

Figure 5 illustrates the model in which the emission current fluctuation originates from the adsorption and desorption of atoms and/or ions. The current fluctuation occurs due to the occupation of the emission sites by the adsorbed atoms. Here, we postulate that the magnitude of the current ($I$) is proportional to the number of occupied states ($n$); e.g., $I(n)=I_0+\eta n$, where $I_0$ is the emission current of un-occupied state, and $\eta$ is the magnitude of the current-hop due to the adsorption of single molecule, to explain both the reduction of the deviation and the lower peak shift of the current distribution. For this model, we define the transition probability of the number of adsorbed atoms from state $E_i$ to state $E_j$ as

$$P_{ij}(t) = P(X(s+t) = j \mid X(s) = i) \tag{2}$$

where $X(s)$ is a random variable at time $s$. We postulate that the system changes only through transitions from states to their nearest neighbors. If at time $t$, the system is in state $E_i$, the probability $[P_{ii+1}(h)]$ that between $t$ and $t+h$ the transition $E_i \rightarrow E_{i+1}$ occurs equals
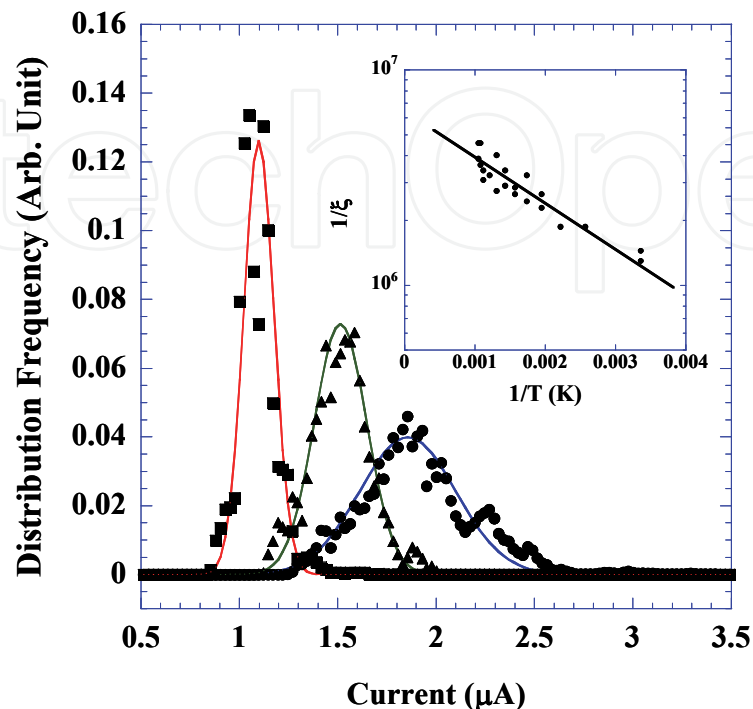


Fig. 4. Histogram of the emission current intensity at 300 K (solid circles), 700 K (solid triangles), and 925 K (solid squares) in a $H_2$ atmosphere; the solid lines are the theoretically fitted curves. The inverse of the variance for each temperature obtained by the theoretical fitting is shown as solid circles in the inset. The solid line in the inset is the fitted curve with a physical adsorption energy of 45 meV. (Reprinted with permission, Matsumoto et al. 2008, American Physical Society.)
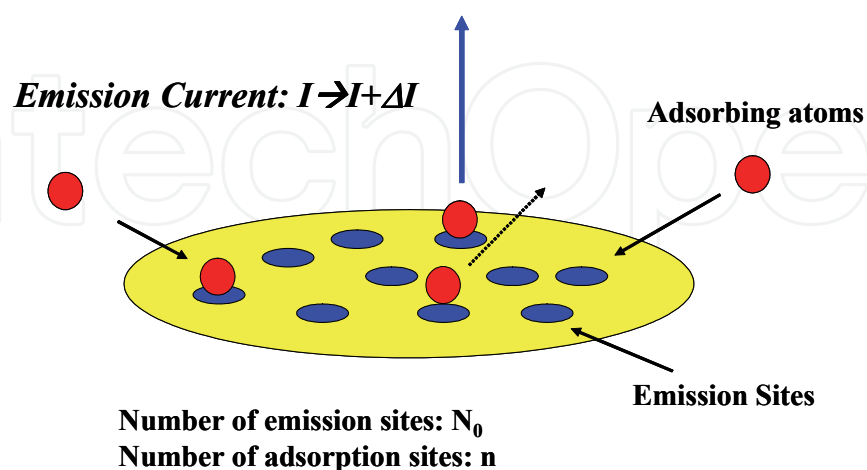


Fig. 5. Physical desorption model in which fluctuation of the emission current originates from the adsorption and desorption of atoms and/or molecules onto the emission sites. (Reprinted with permission, Matsumoto et al. 2008, American Physical Society.)

$\lambda_i h + o(h)$, and the probability $[P_{ii-1}(h)]$ of $E_i \rightarrow E_{i-1}$ equals $\mu_i + o(h)$. The probability that during $(t, t+h)$ more than one change occurs is $o(h)$, where $\lambda_i$ corresponds to the adsorption rate, $\mu_i$ corresponds to the desorption rate, $o(h)$ denotes a small quantity of order of magnitude $h$, and $h$ is the subinterval of time duration $h=1/N$ (N: total interval, and generally $h \rightarrow 0$). That is; the adsorption and desorption rates in state $E_i$ are equal to the sum of three distinct ways as shown in Fig. 6 and they can be written as

$$P_{ii+1}(h) = \lambda_i h + o(h) \tag{3}$$

$$P_{ii-1}(h) = \mu_i h + o(h) \tag{4}$$

$$P_{ii}(h) = 1 - (\lambda_i + \mu_i)h + o(h) \tag{5}$$

$$P_{ik}(h) = o(h) \qquad (|i-k| \geq 2) \tag{6}$$

$$P_{ij}(h) = \delta_{ij} \tag{7}$$

We consider that the adsorption and desorption processes shown in Fig. 5 can be described quantitatively as time-homogeneous Markov processes satisfying the following Chapman-Kolmogorov equation (Feller, 1957);

$$P_{ij}(t+h) = \sum_k P_{ik}(t)P_{kj}(h) \tag{8}$$

By taking $k=j-1, j, j+1$ for the summation in Eq. (8) and using Eqs. (2) to (7), we obtain the following differential equations:

$$\frac{dP_{ij}(t)}{dt} = \mu_{j+1}P_{ij+1}(t) + \lambda_{j-1}P_{ij-1}(t) - (\lambda_j + \mu_j)P_{ij}(t) \tag{9}$$

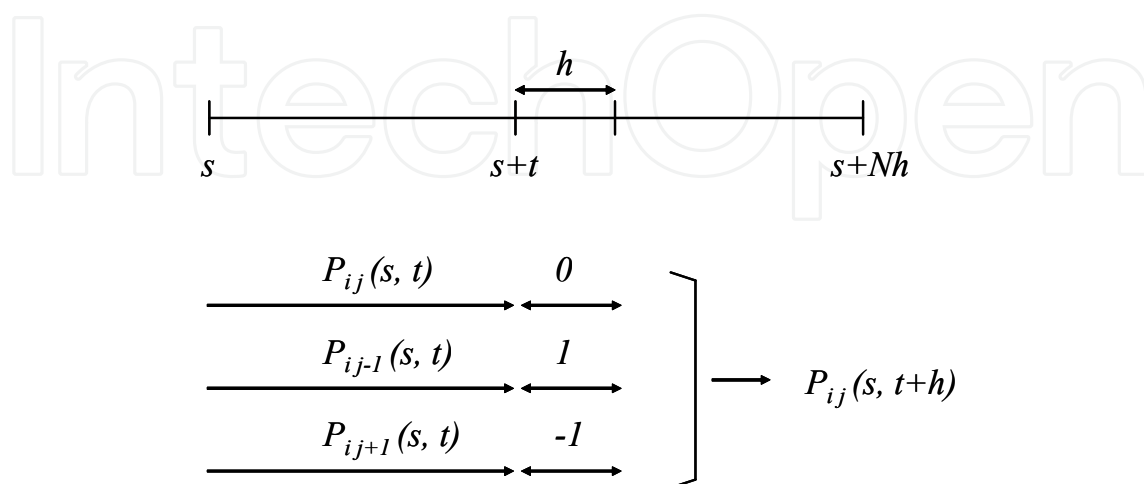$$\frac{dP_{i0}(t)}{dt} = \mu_1 P_{i1}(t) - \lambda_0 P_{i0}(t) \tag{10}$$



Fig. 6. Time intervals used in the calculation of $P_{ij}(t)$ showing the three ways in which j states are adsorbed in the period between $s$ and $s+t+h$.

To describe the adsorption and desorption processes shown in Fig. 5, we assume that the rate $\lambda_j$ is proportional to the number of unoccupied emission sites, while the rate $\mu_j$ is proportional to the number of occupied sites. Defining $N_0$ as the total number of emission sites and $j$ as the number of occupied sites, we set

$$\lambda_j = \alpha (N_0 - j) \tag{11}$$

$$\mu_j = \beta j \tag{12}$$

where $\alpha$ and $\beta$ are constants, such that $\alpha$ depends linearly on both the current density and the residual pressure and $\beta$ depends on the temperature of the cathode. For example, $\beta \propto exp[-E_{ad}/k_B T]$, where $E_{ad}$ is the physical adsorption energy, $T$ is the temperature, and $k_B$ is the Boltzmann constant. Considering the stationary distribution for Eqs. (9) to (12), the limits $\lim P_{ij}(t) = p_j$, $t \rightarrow \infty$, exist and are independent of the initial conditions (Matsumoto et al., 2008). Therefore, Eqs. (9) to (12) can be combined to express the stationary distribution $p_n$ as the following Poisson distribution:

$$p_n = \frac{\xi^n}{n!} \exp(-\xi) \tag{13}$$

where $\xi = N_0 \alpha / (\alpha + \beta)$ and we assume the desorption ratio, $\beta$, is much larger than the adsorption ratio, $\alpha$.

The solid lines in Fig. 4 are the theoretically fitted curves given by Eq. (13), where the best fits were obtained using the fitted values, $\xi = 2.76 \times 10^{-7}$ for 920 K (red line), $\xi = 3.45 \times 10^{-7}$ for 700 K (green line), and $\xi = 7.72 \times 10^{-7}$ for 300 K (blue line). By fitting the histogram of the current fluctuation at various cathode temperatures with Eq. (13), and then plotting these theoretically determined values logarithmically $[ln(1/\xi)]$ as a function of the inverse of the temperature, $1/T$,

$$ln(1/\xi) \propto -E_{ad} \cdot (1/k_B T) \tag{14}$$

we can determine the physical adsorption energy, $E_{ad}$, from the slope, as shown in the inset of Fig. 4. The solid line shown in the inset of Fig. 4 is the theoretical line computed with a physisorption energy of $E_{ad}$ = 45 meV. The adsorption energies of $H_2$ molecules on graphite-like surfaces show a wide range of binding energies from 20 to 80 meV (Jacobson et al., 2002; Tran et al., 2002) because the adsorption energy of molecules on the carbon nanostructures varies as the size (e.g., the tube diameter), coordinate sites, and the surface structure of the carbon nanomaterials change. We cannot distinguish the adsorption sites of the $H_2$ molecules onto the emission sites of the carbon nanostructures; however, the physisorption energy of $E_{ad}$ = 45 meV is similar to the energy onto a graphite surface (Vidali et al., 1991).

The error obtained by this method is within ±5 meV, which allows the determination of the physisorption energy of various molecules to a high degree of accuracy. Figure 7 shows the values of $1/\xi$ obtained by measuring the emission current fluctuations as a function of various temperatures for CO (green circles), Ar (blue squares), and He molecules (red triangles). The slope of the solid line shows the theoretically determined physical adsorption energies, $E_{ad}$: 110 meV for CO molecules, 100 meV for Ar, and 15 meV for He. These graphene nanoneedle physisorption energies are similar to the physisorption energies for the graphite surface (Vidali et al., 1991).

We cannot rule out the possibility that the current fluctuation occurs due to variations in the adsorbate coverage on step edges and defects, where the enhancement of physisorption energy occurs (Ulbricht et al., 2002; Ulbricht et al., 2006). However, polar adsorbates such as CO molecules on the graphite nanostructure showed similar adsorption energy to those on the graphite basal surface, and we did not observe enhancement of the binding energy due to a dipole interaction between polar molecules and step edges or defects. Therefore, we consider that the electron emission occurs not from the edge of the nanoneedle, but from the basal plane of the graphene sheet. Next section, we will study the emission mechanism of graphene nanoneedles from the point of view of the nanometer sized region by using field emission and field ion microscopes.
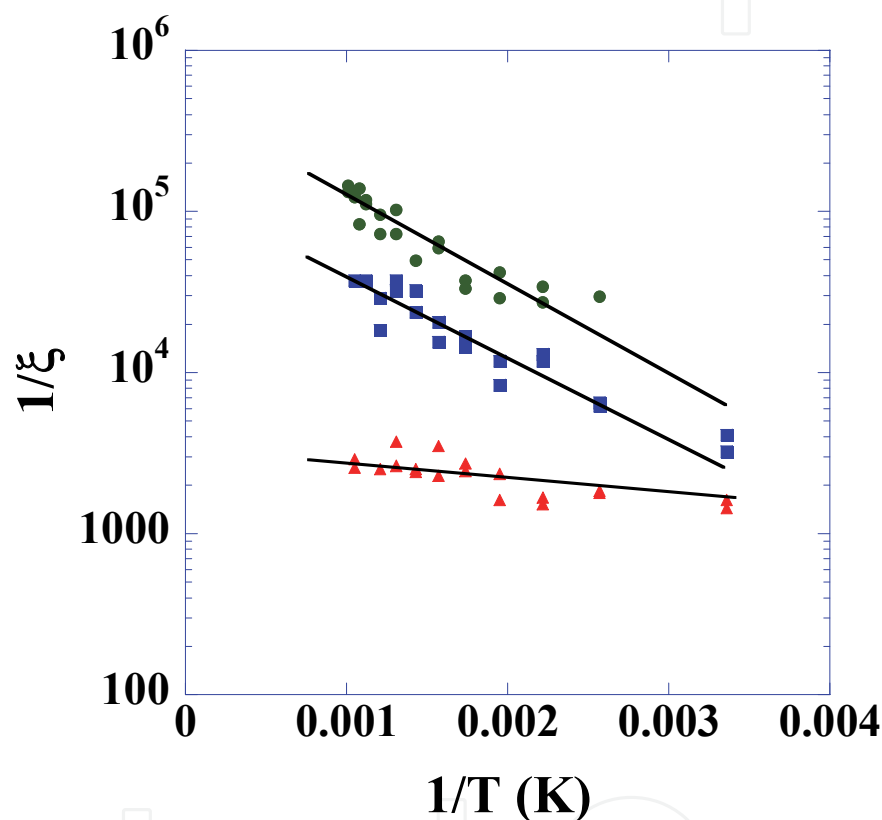


Fig. 7. Inverse of the variance, $1/\xi$, for CO molecules (green circles), Ar molecules (blue squares), and He molecules (red triangles) as a function of GNS cathode temperature. The solid lines are the fitted curves with physical adsorption energies of 110 meV for CO molecules, 100 meV for Ar, and 15 meV for He. (Reprinted with permission, Matsumoto et al. 2008, American Physical Society.)

## 5. Microscope images of emission patterns and their quantum states

### 5.1 Field emission and field ion microscope images
In section 4, we simply measured the total current (the ensemble of the emission sites) and discussed the statistical dynamics by using a stochastic differential equation. In this section, the ensemble of the emission sites will be resolved into a number of single emission site by using a field emission microscope (FEM) and a field ion microscope (FIM). We show that each emission site of GNS creates many beautiful symmetrical patterns. These symmetrical

patterns are known as cloverleaf patterns of organic molecules and the origin of the cloverleaf patterns has been discussed more than 60 years; however, this is still open question (Müller, 1953; Ashworth, 1951; Dyke & Dolan, 1956; Becker, 1955; Wolf, 1955; Dean, 2002). In order to solve this difficult problem, we try to reproduce the same cloverleaf patterns by using historically used organic molecules such as phthalocyanine and pentacene. By considering phase information for the obtained symmetrical patterns, which is a first attempt to explain these symmetrical patterns, and by applying the diffraction analysis to the tunneling electron observed by FIM (near field wave function), we succeed in explaining how the near field pattern obtained by FIM changes into the far field pattern obtained by FEM. Our final conclusion for the cloverleaf pattern is that the electron emission originates from anti-bonding states (lowest unoccupied molecular orbital) of $\pi$-conjugated bonds (six-membered ring) in the graphene sheet (Neo et al., 2010).

Our ultra-high-vacuum experimental apparatus includes both FEM and FIM chambers. In order to obtain the same information for FEM and FIM, FEM and FIM measurements were successively performed through a load-lock and a preparation chamber in order to avoid exposure to air. The base pressures in the FEM and FIM chambers are below $1 \times 10^{-7}$ Pa and $2 \times 10^{-8}$ Pa, respectively. The FEM apparatus consists of a field emission cathode mounted on an x-y-z-manipulator, a phosphor screen, and an evaporation boat to adsorb organic molecules onto a tungsten tip. A GNS structure and an electrically-polished tungsten (011) tip were attached to 0.15 mm diameter tungsten filaments. It is possible to heat the cathode by resistive-heating of a tungsten filament. A phosphor screen on an ITO glass substrate was placed in front of the tip in the FEM chamber, with a 50 mm gap. The adsorption processes of the organic molecules were monitored in-situ by observations of FEM images. The adsorption conditions were easily controlled by adjusting the boat temperature and hence its vapor pressure. The FIM chamber consists of a helium cryo-cold head and a micro-channel plate (MCP). The MCP with a phosphor screen was placed 50 mm in front of the cathode. The cathode was cooled by a cold head up to 9 K. Two variable-leak valves were included in order to introduce helium and hydrogen gas molecules as imaging particles under FIM operation. The FEM and FIM images were recorded using a charge-coupled device (CCD) camera.

After flash-heating for a few minutes at around 1000 K, field emission could typically be initiated in our FEM apparatus, even when low voltages of less than -2 kV were applied to the cathode. Figure 8 (a) shows a phosphor screen image of the electrons emitted from a GNS cathode, and it can be observed that each of the bright-spots shows symmetrical patterns such as two-lobed, four-lobed, circle and ring patterns as shown in Fig. 8 (b). These patterns exhibit some of the following tendencies; (i) each of the patterns could rotate discontinuously and (ii) could change reversibly into another pattern. (iii) Interestingly, no patterns with an odd number of lobes (e.g. three-lobed patterns) were observed. (iv) The two parts of each two-lobed pattern and the four parts of each four-lobed pattern were always symmetrical, had the same brightness, and vanished at the same time. These behaviors of the cloverleaf patterns were similar to those observed for other types of organic molecules such as phthalocyanine and pentacene, and we will show similar symmetrical patterns obtained by these molecules in Fig. 10.

After the FEM investigations, the GNS emitter was transferred to the FIM chamber. The emitter was cooled to 25 K, which was above the hydrogen triple point. Hydrogen up to a pressure of $1 \times 10^{-2}$ Pa was introduced into the FIM chamber as an imaging gas, and then high positive voltages were applied to the GNS cathode. Figures 9 (a), (b) and (c) show the

successive FIM images in a sequence in which the tip voltage was increased up to +10 kV. In the high-voltage region (over +10 kV) bright lines due to reflected multi-layers structures (Williams, 1968; Murr & Inal, 1971) were observed, as shown in Fig. 9 (c). However, in the weak-field region, the cloverleaf patterns observed in the FEM images, were also appeared in the FIM measurements. Figure 9 (d) shows a collection of the patterns such as those observed in the weak region (around +5 kV). These patterns were almost the same as the cloverleaf patterns obtained in the field emission regime. The same symmetrical patterns obtained by both FEM and FIM are interesting because the FIM gives the near field images such as the wave function of tunneling electron, while the FEM gives the far field images.
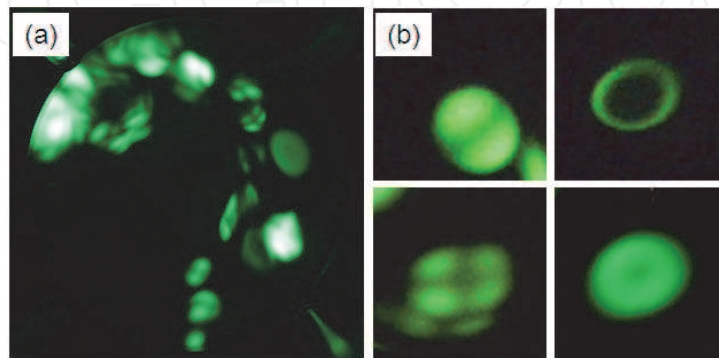


Fig. 8. (a) FEM images of a GNS cathode on a phosphor screen at 2.2 kV applied voltage, (b) the four typical kinds of cloverleaf patterns observed with GNS; two-lobed, four-lobed, ring and circle. (Reprinted with permission, Neo et al. 2010, American Institute of Physics.)
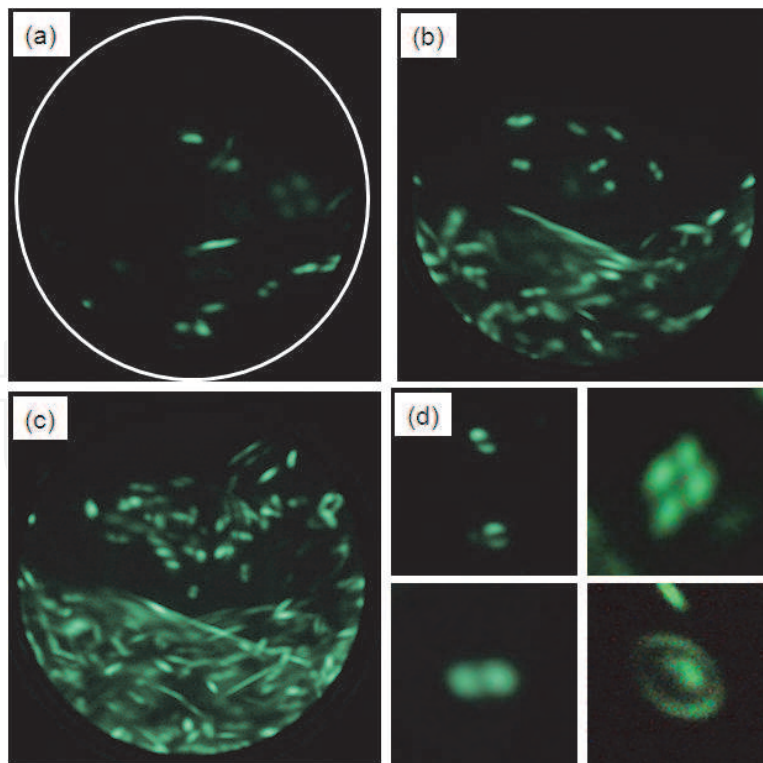


Fig. 9. A series of FIM images obtained with GNS in a sequence of increasing applied voltages; (a) 4 kV, (b) 5 kV, (c) 10 kV. (d) Collection of typical FIM patterns. (Reprinted with permission, Neo et al. 2010, American Institute of Physics.)

## 5.2 Field emission and field ion microscope images of Cu-phthalocyanine (Cu-Pc) and pentacene

We observed various symmetrical FEM and FIM patterns in GNS emitters such as two-lobed, four-lobed, circle and ring patterns. The patterns observed in GNS are very similar to those previously-observed in organic small molecules such as pentacene and Cu-Pc. Here we reproduce the cloverleaf patterns by the evaporation of pentacene and Cu-Pc onto a tungsten tip.

An electrically-polished tungsten (011) tip was mounted and an evaporation boat containing small quantities of these molecules was equipped in the FEM chamber. After cleaning the tungsten surface by heating to around 2200 K for 30 seconds, the evaporation boat was heated electrically, and then the field emission occurred from the clean tungsten surface. When several cloverleaf patterns appeared on the phosphor screen, the electrical heating of the evaporation boat was stopped. Figures 10 (a) and (b) show the cloverleaf patterns of FEM obtained in pentacene and Cu-Pc, respectively. The insets in the figure indicate the typical patterns that were observed for each molecule. As was observed in GNS, the same two-lobed, four-lobed, circle and ring patterns were observed in both organic molecules, especially clearly observed in Cu-Pc (Müller, 1953). The FEM images of these molecules, representing far field pattern of electron wave, show the same symmetrical patterns as those observed in GNS structures.
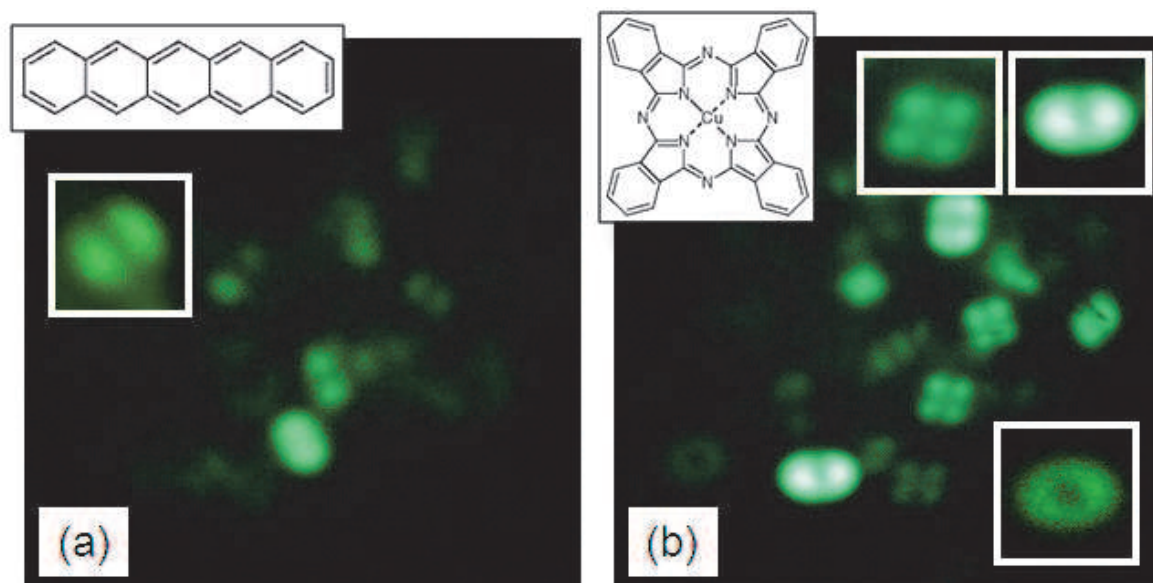


Fig. 10. FEM images with (a) pentacene and (b) Cu-Pc, respectively. The insets indicate the molecular structures and the cloverleaf patterns typically observed in FEM. (Reprinted with permission, Neo et al. 2010, American Institute of Physics.)

The electronic states of the emission sites (near field images) for pentacene and Cu-Pc were also investigated using the FIM method. Figures 11 (a) and (b) show the collected FIM patterns that were observed with pentacene and Cu-Pc, respectively. The observation of the cloverleaf patterns were performed at low electric field region around +4 kV. This value was much lower than that observed for the FIM images of tungsten surface (over +10 kV) because the adsorbed molecules are easily desorbed by the high electrical field. For pentacene, two-lobed patterns were mainly observed; on the other hand, two- and four-lobed patterns were clearly observed for Cu-Pc. These results agree well with the tendencies

that were observed in a series of FEM measurements. However, the agreement between the near field FIM patterns and the far field FEM patterns is not obvious and contains interesting information because the electron wave function tunneling through these molecules will be distorted by diffraction. That is, the FIM probes the electronic states of the near field emission region, while the FEM shows a far field pattern of the diffracted electron wave function emitted from the nanometer sized region. It looks like a contradiction; however, if we consider phase information for the symmetrical patterns, we show that this agreement is physically natural when we consider the emission originating from the anti-bonding states. Next, we will theoretically analyze the symmetrical patterns (wave function) by adding the phase information. We will analyze the near field and the far field patterns based both on the principle of least action and on the diffraction of the electron wave optics.
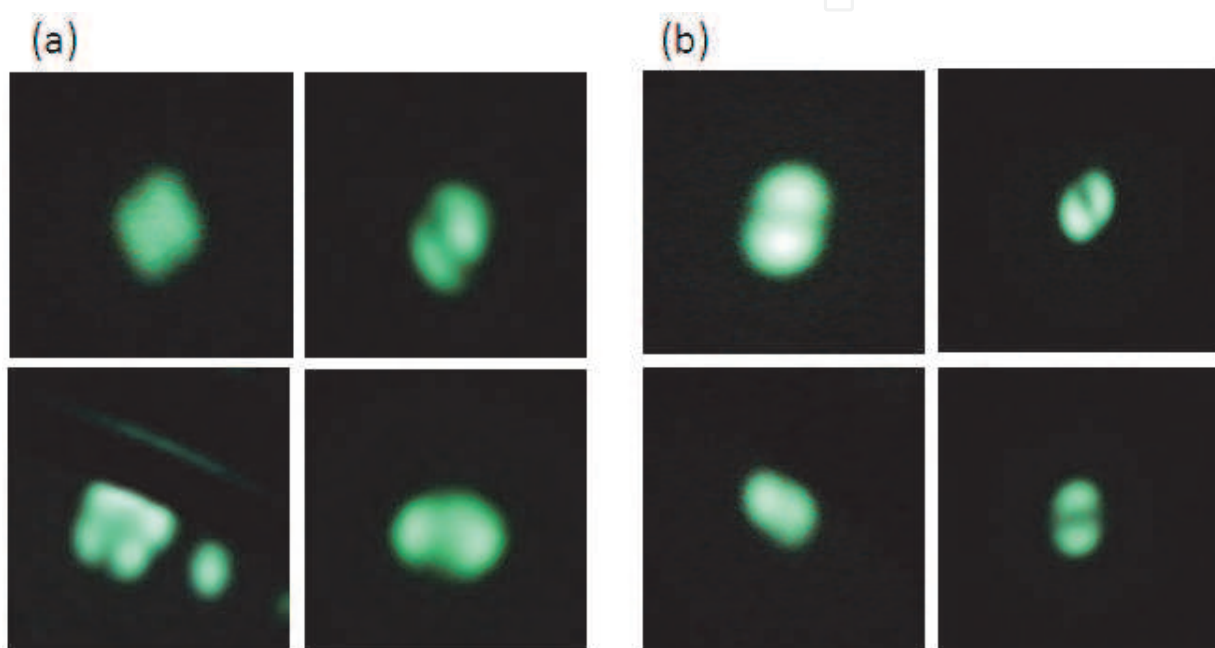


Fig. 11. Collection of cloverleaf patterns observed at around +4 kV with (a) Cu-Pc and (b) pentacene. (Reprinted with permission, Neo et al. 2010, American Institute of Physics.)

### 5.3 Diffraction of tunneling electron

Here electron wave optics is applied to analyze both the FEM and FIM patterns. The theoretical description of electron wave optics is almost the same as that of electromagnetic wave optics (Born & Wolf, 1999). The difference between the electron optics and optics is the treatment of wavevector, and in the electron optics, wavenumber depends on the potential. However, qualitatively, both the electron optics and optics give almost the same formalism in spite of the difference of the phase (wavenumber) treatment. The key to understand diffraction images is a popularly known Fourier transformation. The detail of the electron wave optics was given in the following papers (Couley, 1995; Ximen, 1994) and here we show final expression. The dffracted electron beam can be expressed by the convolution of the near field wave function and the spherical wave as

$$\Psi(x_2, y_2) = A(\Phi, z) \iint dx_1 dy_1 \, \Psi(x_1, y_1) \, \frac{z_{12}}{r_{12}} \, \frac{e^{i\vartheta}}{r_{12}} \tag{15}$$

where $\Psi(x_1, y_1)$ is the electron wave function obtained by FIM pattern (near field image at $x_1$ and $y_1$ with phase information), $\Psi(x_2, y_2)$ is the electron wave function obtained by FEM pattern (far field image at $x_2$ and $y_2$ with phase information), $A(\Phi, z)$ is the amplitude determined by Schrödinger equation with electron potential $\Phi$, $z_{12}/r_{12}$ is the obliquity factor where $r_{12}$ is the distance between $(x_2, y_2, z_2)$ and $(x_1, y_1, z_1)$, and $z_{12} = |z_2 - z_1|$, and $e^{i\vartheta}/r_{12}$ is the spherical wave of which phase $\vartheta$ is determined by the motion of electron in a potential. By applying the principle of least action, this phase can be expressed as a simple form like $\vartheta = k_0 r_{12} + \varphi(z)$ where $k_0 = [2em\Phi(z_1)]^{1/2}/\hbar$ is a wavenumber of electron wave at $z = z_1$ and $\varphi(z)$ can be treated as a constant value in this diffraction process. At Fraunhofer region as shown in Fig. 12, Eq. (15) becomes a Fourier transform relation between the near field pattern and the far field pattern as

$$\Psi(x_2, y_2) \propto \iint dx_1 dy_1 \, \Psi(x_1, y_1) \, exp\left[\frac{ik_0}{z_{12}}(x_1 x_2 + y_1 y_2)\right] \tag{16}$$

Therefore, we can calculate the near field pattern from the far field pattern or vice versa easily by using the Fourier transform relation obtained in Eq. (16).

Next we consider the phase of the wave function because the intensity measurements of FEM and FIM do not contain phase information. If we consider the phase for the obtained two-lobe patterns of FIM, we can consider two cases; each lobe has the same in-phase or different anti-phase. Figure 13 shows theoretically computed results for two-lobe pattern of (a) in-phase and (b) anti-phase. When the two-lobes have the same phase, calculated far field image becomes an intense circular spot with side bands ringing. On the other hand, when the two lobes have the anti-phase, interestingly, calculated far field image becomes topologically the same as that of near field image. We also show the calculated results for four-lobe patterns in Fig. 13 (c) in-phase and (d) anti-phase. The agreement between the near field FIM patterns and the far field FEM patterns indicates that the electron wave function tunneling through these molecules has the anti-symmetrical phase. Based on our series of FIM and FEM measurements for various molecules including Cu-Pc and pentacene, π conjugated bonds are essential to form the symmetrical patterns. The anti-symmetry of π conjugated bonds naturally suggests the conclusion that the symmetrical leaf pattern originates from the lowest unoccupied molecular orbitals.

Many symmetrical patterns were observed in various organic molecules with π conjugated bonds, such as six-lobed and ring patterns as well as the two- and four-lobed patterns. It is interesting to consider these patterns by correlating with the π conjugated bonds of six membered ring. By considering the confinement states in a cylindrical coordinate, that is, by solving the Schrödinger equation in this boundary condition, we can obtain following wave function described by Bessel function as

$$\Psi_{nm}(r, \theta) \propto \frac{1}{|J_{n+1}(\xi_{n,m})|} J_n(\xi_{n,m} \cdot r / r_0) \, exp(in\theta) \tag{17}$$

where coordinate is transformed from Cartesian coordinate to the cylindrical coordinate, n is the mode number, m is the order number, $J_n(\xi_{nm})$ is the nth order Bessel function and $\xi_{nm}$ is the mth value of the solution of $J_n(\xi_{nm}) = 0$. By solving Eq. (17), we can obtain wave functions at the near field region. Figure 14 shows the experimentally observed symmetrical

patterns, the solution of the wave function for lower quantum numbers, its intensity (square of the wave function), and the calculated far field intensity obtained by Fourier transformation. Almost all the patterns obtained by both FEM and FIM measurements were reproduced by this computing analysis of Eq. (17). The difference of the observed patterns originates from the difference of the energy level of $\pi$-electron at excited states (LUMO states).
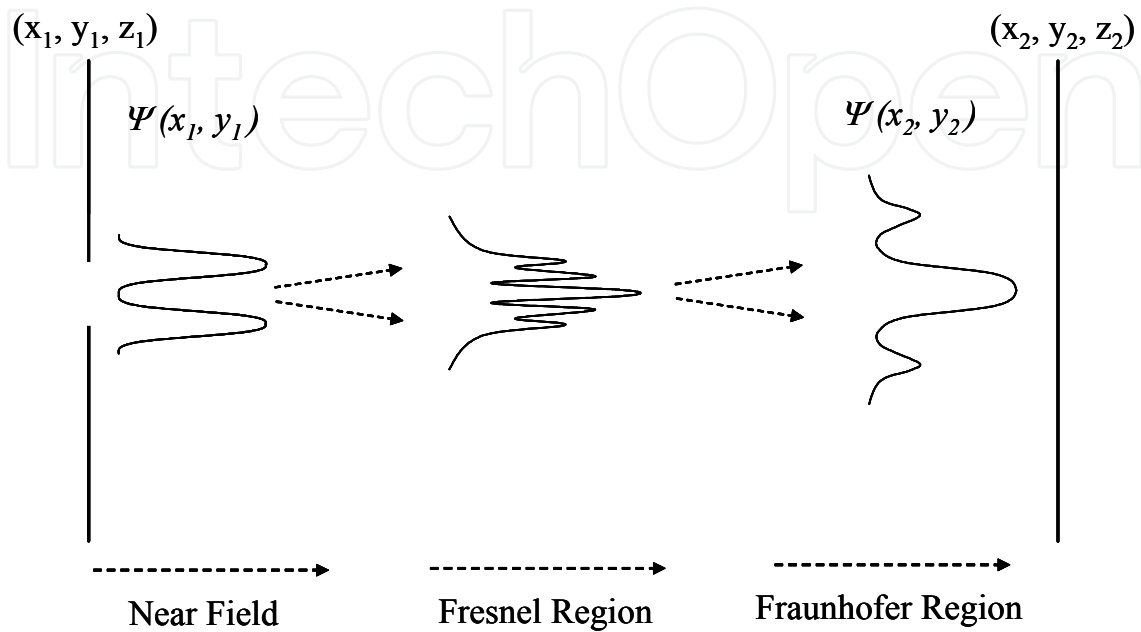
$(x_1, y_1, z_1)$ $(x_2, y_2, z_2)$

$\Psi(x_1, y_1)$ $\Psi(x_2, y_2)$

Near Field Fresnel Region Fraunhofer Region

Fig. 12. Schematic image of the diffraction of electron wave and the change of the wave function from near field to far field (Fraunhofer region).

| | (a) Two Lobes in phase | (b) Two Lobes anti phase | (c) Four Lobes in phase | (d) Four Lobes anti phase |
|---|---|---|---|---|
| **Wave function at near field** | | | | |
| **Intensity at near field (FIM pattern)** | | | | |
| **Intensity at far field (FEM pattern)** | | | | |

Fig. 13. Theoretically calculated near field and far field intensities for two-lobes and four-lobes patterns. The phase of the wave function is introduced as in-phase [(a) and (c)] or anti-phase [(b) and (d)].

Quantitative discussion related with the magnitude of the energy difference for the different quantum number is necessary to be clarified; however, qualitatively, adsorbed or desorbed atoms on and off π conjugated ring cavity (emission sites) would change the energy level of the cavity modes, thus the patterns rotate discontinuously and change reversibly.

We note here, the quantum number n is degenerated; however, when the degeneracy is solved by the existence of a magnetic moment and/or a localized spin near the π conjugated cylindrical cavity, we can expect topologically interesting patterns such as an entangled pattern of electron wave function for FEM measurements (Müller, 1953; Ashworth, 1951; Dyke & Dolan, 1956; Becker, 1955).

The mystery of the same topological patterns between FIM and FEM were clearly solved by considering the phase of the electron wave function for both FIM and FEM patterns, and quantitatively analyzed by using the electron wave optics. The various emission patterns observed in GNS have the same origin as those observed in organic molecules, where the symmetrical patterns can be understood from the point of view of the excited states of the π electron of six membered ring in a two dimensional graphene sheet. Therefore, the patterns have the same brightness, and vanish at the same time. Furthermore, odd number of the lobe-pattern is prohibited to be appeared due to the confinement of cylindrical cavity. The change of the patterns can be understood from the point of view of the change of the energy level by the adsorption of atoms or molecules on and off the six membered ring. Coherence of the tunnelling electron from a two dimensional graphene sheet is regarded as high because there is no inelastic scattering process. Thus, we consider that the graphene is a promising candidate for a coherent electron source. Many new physics unfold before us such as the superposition of coherent electron emission from a graphene sheet, opening a way for making a plane wave and an amplification of electron beam.
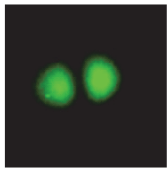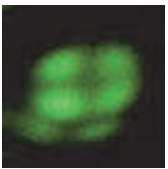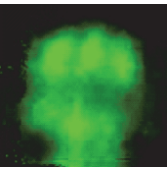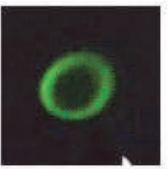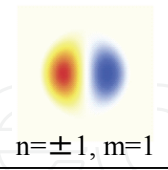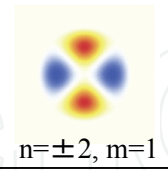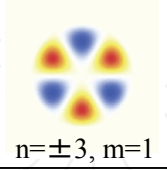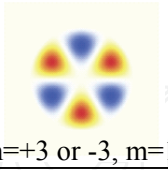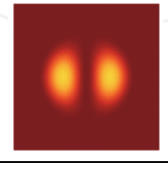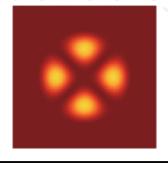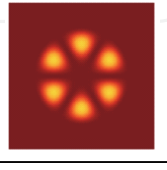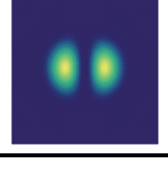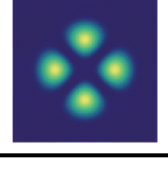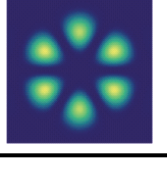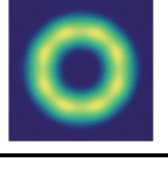
| | (a) Two Lobes | (b) Four Lobes | (c) Six Lobes | (d) Ring |
|---|---|---|---|---|
| **Observed Patterns** | | | | |
| **Wave function at near field and quantum number** | n=±1, m=1 | n=±2, m=1 | n=±3, m=1 | n=+3 or -3, m=1 |
| **Intensity at near field (FIM pattern)** | | | | |
| **Intensity at far field (FEM pattern)** | | | | |

Fig. 14. Experimentally observed cloverleaf patterns and theoretically calculated wave functions, near field intensity, and far field intensity.

## 6. Applications

### 6.1 X-ray applications

Recently achieved electron emission from carbon nanotubes (CNT) and diamond films show promising aspects due to their possible use in practical cold cathode for the applications such as flat panel displays, x-ray tubes, and microwave amplifier. However, these emission sources still have problems related to adherence of the interface between carbon layers and its substrate. Furthermore, the advantage of a high gas storage capacity of CNT acts as disadvantage for the fabrication of highly evacuated vacuum devices.

We overviewed superior aspects of field emission properties in GNS cold cathode. Especially, unsaturated behavior of electron emission and stable emission in a high residual pressure region of the order of $10^{-4}$ Pa (We will introduce the results of the emission stability later in the FE-SEM section.) are distinguishing characteristics compared to other types of carbon emitters. This is due to the fabrication of carbon nanostructure onto a carbon substrate. Both the high current density and the stable emission characteristic are desirable for high power operation of devices such as x-rays, electron microscopes, and microwave generators. In this section, we show the performance of the GNS as a cold cathode was demonstrated by various applications. Firstly, we show the results of high intensity and short pulse x-ray generation and then introduce the demonstration of stop motion of x-ray transmission images. Fast motions of the order of 10 μs are obtained by using GNS cathode in a convenient manner. Secondly, we will introduce the fabrication of miniature sized x-ray tubes with the GNS emitter. Long lifetime of the order of 10,000 hours and the stability better than 1 % are emphasized. We believe that this x-ray tube is the first commercial base application using a graphene technology. Lastly, we show the results of the stable emission from GNS in a high residual pressure region, which is suitable for the construction of field emission type scanning electron microscope with a convenient manner.

Figure 15 (a) shows a schematic of a triode-type field emission x-ray tube composed of a GNS cathode, a metal grid (100-mesh placed 0.5 mm from the cathode), and a Cu metal target. The x-ray tube was evacuated by a turbo-molecular pump to a base pressure of $10^{-4}$ Pa. For pulse x-ray generation, negative pulse voltage with a peak height of 1-10 kV and pulse duration between 1 ms and 10 μs (repetition 1-100 Hz) was applied to the cathode. The metal grid was grounded and a constant positive bias of about 20 kV was applied to the anode. Figure 15 (b) shows the pulse voltage applied to the GNS cathode (pulse duration of 1 ms; dotted line) and generated x-ray pulses (solid line) detected by $Gd_2O_2S:Eu$ phosphor with a photomultiplier. High intensity x-ray pulse was obtained by applying a negative pulse voltage to the cathode. A 1-ms-pulse duration for the applied voltage was used, because the response of our detection system was limited by the phosphor decay, which was about 500 μs. A much shorter x-ray pulse, on the order of 10 μs, was generated and by using this pulse we demonstrated in the following two applications that the GNS cold cathode can be used for high speed x-ray radiography.

In the first application, Fig. 16 (a) shows single-shot x-ray transmission image of a rotating chopper (7500 rpm) obtained by placing the chopper between the pulse x-ray emission source and a cooling type charge coupled device camera (CCD) with a $Gd_2O_2S:Eu$ phosphor. The image was obtained at an applied anode bias of 25 kV (DC) and a cathode bias of -10 kV. Based on the angular velocity of the rotating chopper and the sharpness of the obtained image, the generated x-ray pulse duration was estimated to be about 10 μs.

In the second application [Fig. 16 (b)], in situ image of a rotating drill and the process of making a hole inside a wood plate were obtained using the same condition used in the first

application. For this demonstration, we used a 2 mm-diameter drill (2600 rpm) and a 5-mm-thick wood plate. Images were obtained of the rotating drill moving inside of the wood plate, where this frame was detected by a single shot x-ray flush (10 μs duration). The advantage of the single shot x-ray detection is that clear dynamical transmission images of a fast motion can be obtained without the use of a sophisticated high-speed camera.

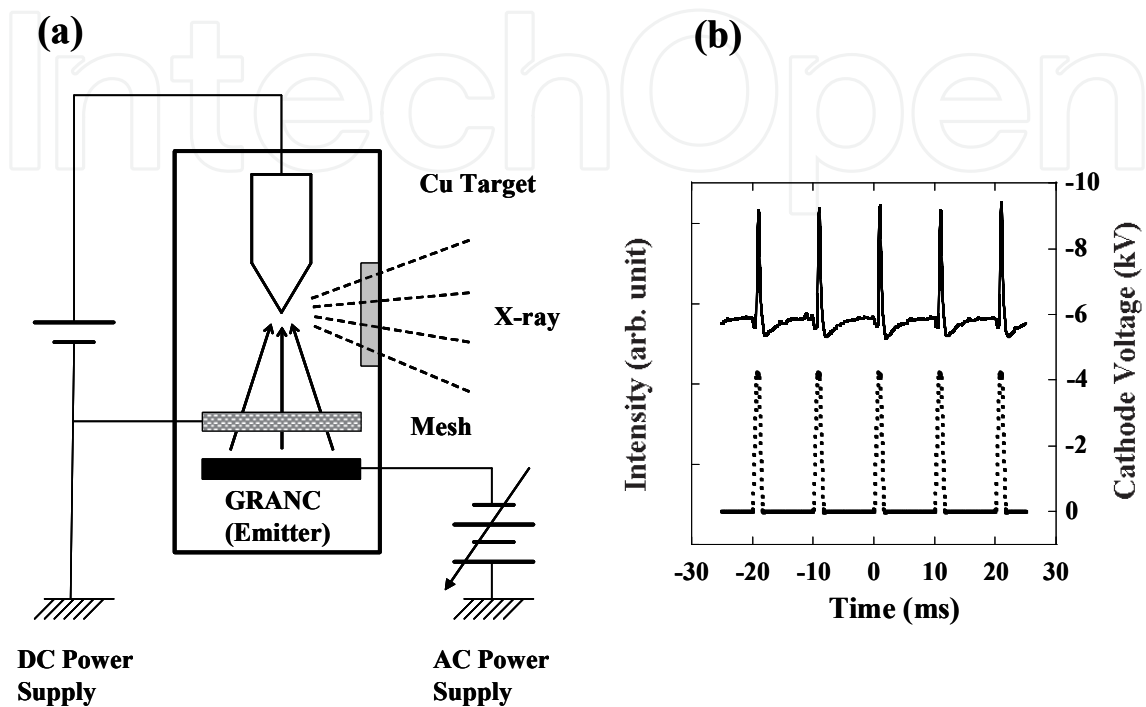**(a)**                                                                      **(b)**



Fig. 15. (a) Schematic of a triode-type field emission x-ray tube, and (b) generated x-ray pulses. (Reprinted with permission, Matsumoto et al. 2004, American Institute of Physics.)

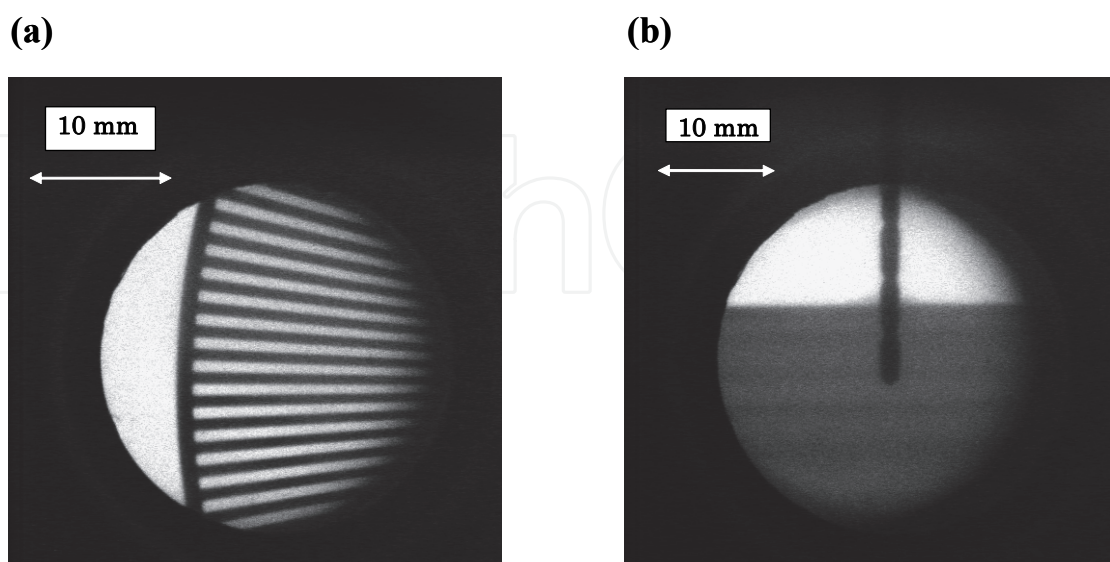**(a)**                                                      **(b)**



Fig. 16. Single shot x-ray transmission images of (a) rotating chopper (7500 rpm) and (b) rotating drill (2600 rpm) moving inside of the wood plate. (Reprinted with permission, Matsumoto et al. 2004, American Institute of Physics.)

## 6.2 X-ray tube fabrications

Bright and stable field electron emission from GNS seems to be promising to construct an x-ray vacuum tube from the point of view of a long longevity and a low power consumption as well as a high spatial resolution and the high speed transmission images compared to a conventionally used x-ray tube with thermal cathode (filament). In this section, we introduce our recent progress in the fabrication of a miniature sized x-ray tube with the GNS (Jyouzuka et al., 2010).

Figure 17 (a) shows a photograph of a fabricated miniature sized x-ray tube with GNS cathode. The size of the x-ray tube was 2.4 cm φ x 7 cm long. X-ray radiation was obtained through a Be window. The evacuation of the x-ray tube is important and this is performed by a turbo-molecular pump to a base pressure of less than $10^{-7}$ Pa. The bakeout temperature was above 300 °C. After the aging process, the x-ray tube was tipped off from the evacuation system. Figure 17 (b) shows the current-voltage characteristics of a typical x-ray tube with a GNS cathode. The GNS cathode was grounded and positive bias was applied to the Be window (anode). The distance between the cathode and the anode is about 1 mm. The emission current increased drastically at the applied voltage of 5 kV and the emission current exceeds 1 mA at the applied voltage of 8.5 kV. A high current from GNS offers a high power x-ray tube in a compact manner.

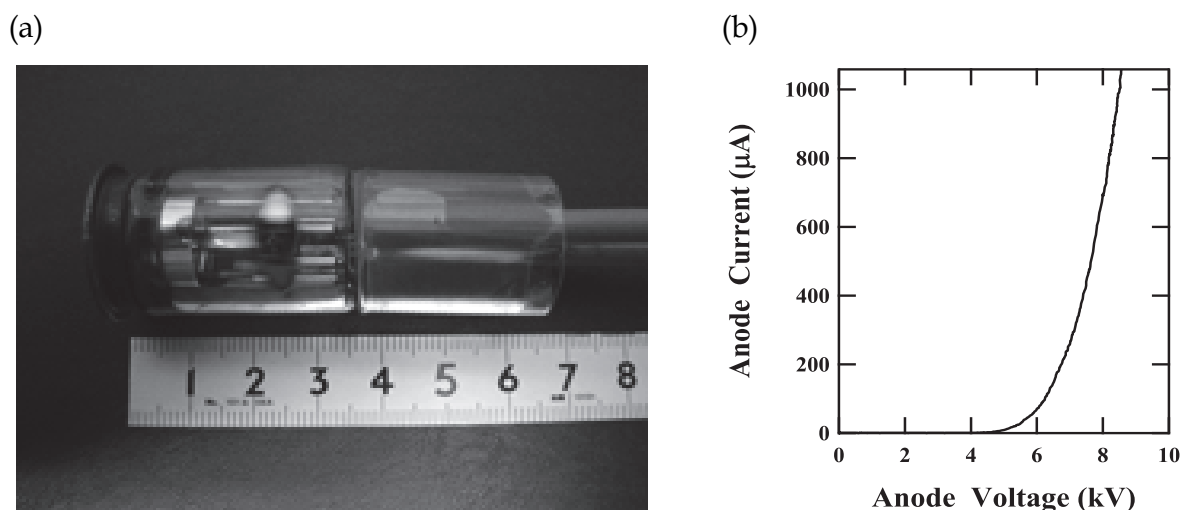(a)                                                                (b)



Fig. 17. (a) Photograph of a miniature sized x-ray tube with GNS cathode. (b) Current-voltage characteristics of an x-ray tube with GNS cathode. (Reprinted with permission, Jyouzuka et al. 2010, American Institute of Physics.)

As described in section 4, the current stability depends on the degree of vacuum level. To stabilize the emission current technically, we here employ a feedback system. The electric feedback diagram of the power supply is shown in Fig. 18 (a). The electric circuit supplies a negative high voltage to the GNS and the anode is grounded. The emission current from GNS is monitored by the current monitor connected to the GNS cathode. In order to stabilize the emission current, the feedback circuit receives the signal from the current monitor and then controls the control gate voltage. We note here that the control gate supplies a negative voltage which is possible to control the field enhancement factor of the GNS cathode. Figure 18 (b) shows the time dependence of the emission current (-20 kV) without (upper) and with (lower) the feedback control described above. Here we set an emission current less than 100 μA in order to make a noisy state of the emission current. In the measurement without the feedback control, the initial emission current was set at 50 μA.

A large noise current was observed and the deviation is estimated to be 7.7 μA. By operating the feedback control, we succeeded in reducing the noise current drastically, as shown in the lower figure of 18 (b) where the same voltage of –20 kV was applied to GNS. The emission current from GNS was set to be the same value of 50 μA. The large noise was significantly reduced and the deviation becomes 0.54 μA. Furthermore, no current flowing into the control gate was observed, implying that the control of the electric field (field enhancement factor) offers a very promising (efficient and fast speed) feedback method to stabilize the emission current in a simple manner.
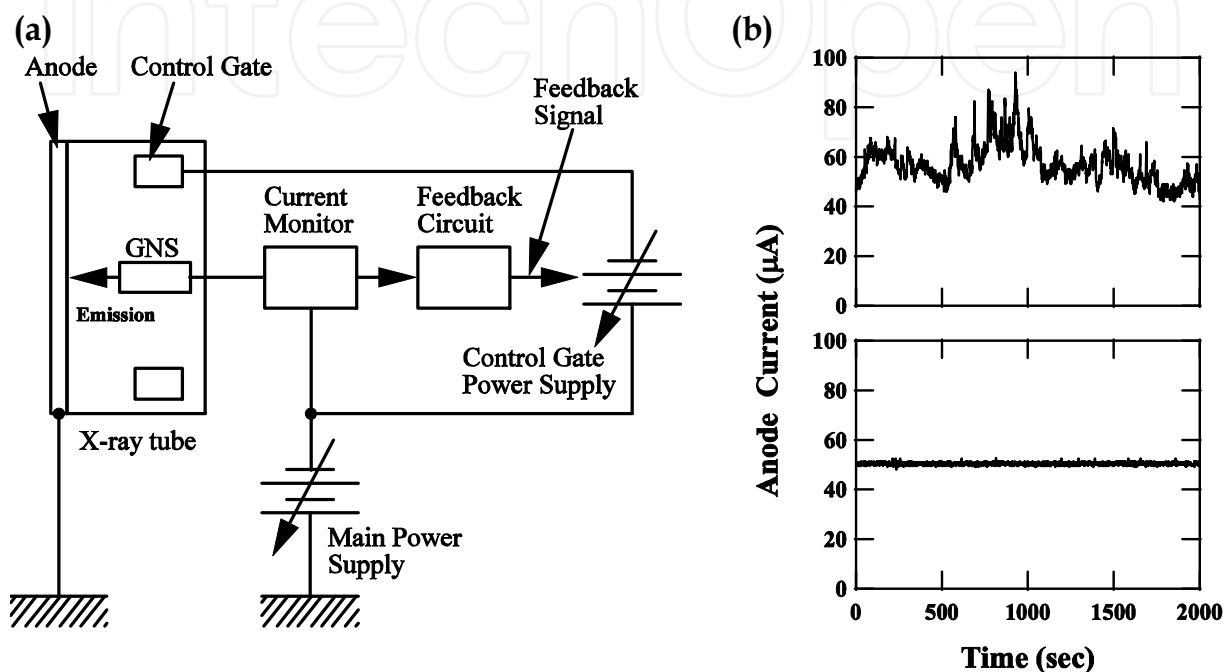
Fig. 18. (a) Feedback circuit to stabilize the emission current. (b) Time dependence of the emission current fluctuation without (upper) and with (lower) the feedback control. (Reprinted with permission, Jyouzuka et al. 2010, American Institute of Physics)
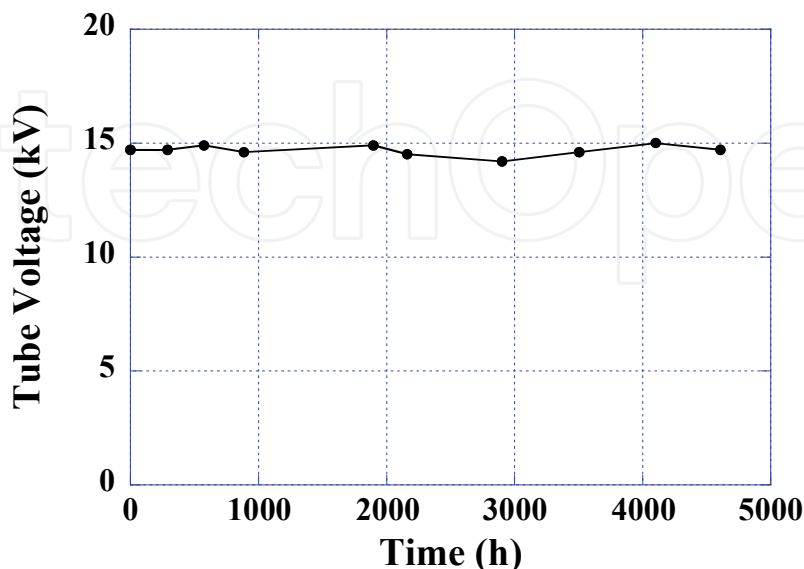
Fig. 19. Lifetime testing of the x-ray tube at constant emission current mode of 500 μA.

Lastly, we show the lifetime of the x-ray tube. Figure 19 shows the time dependence of the applied voltage at the constant current condition of 500 μA. We observed no degradation in the anode bias voltage to maintain the constant current and the lifetime of our x-ray tubes exceeds 5,000 h. The lifetime testing of the x-ray tube is now successively undergoing and it would exceed more than 10,000 h. Both the high emission current more than 1 mA, lifetime more than 10,000 hours, and the stability better than 1 % show very promising aspects of graphene emitters.

## 6.3 FE SEM applications

Intense electron emission at a high residual pressure of $10^{-4}$ Pa seems to be promising to construct a high-resolution electron microscope system without the need for a massive ultrahigh vacuum system. In this section, we show the performance of the GNS as a cold cathode was demonstrated by the construction of a compact FE scanning electron microscope (FE-SEM) system, where the brightness of the GNS cathode was determined to be on the order of $10^{12}$ $Asr^{-1}m^{-2}$ (Neo et al., 2006; Matsumoto et al, 2007).

A schematic of an SEM optical system equipped with a GNS cathode is shown in Fig. 20. The SEM experiments were performed under a residual pressure of about $10^{-4}$ Pa. This pressure was much higher than that of typical FE-SEM with a tungsten tip, which generally requires a low residual pressure, below $10^{-7}$ Pa. Either GNS or a tungsten filament thermal emission (TE) cathode was mounted on the SEM system. Electrode 1, shown in Fig. 20, was used as a wehnelt for a TE cathode and as an extracting gate electrode (0.1-1 kV) for a FE cathode. Other electrodes, such as a suppressor to focus the electron beam, were not included in this SEM system. A single final objective lens was used to focus the crossover on the target (sample holder), where the electron beam diameter and convergence angle were measured. The objective lens was composed of a permanent magnet and assistant coil and was designed to focus at 3.0 kV acceleration voltage. The aperture diameter was 0.3 mm-ϕ. The spatial resolution was evaluated by obtaining the images of a 4 μm-wide copper mesh located on the sample holder. In this lens configuration, the source size was reduced to 0.182 times at the sample target. In addition, a Faraday cup on the sample holder was used to collect the probe current.

Figure 21 (a) shows the SEM image of the copper mesh obtained using the TE cathode to compare both the resolution and brightness with those of the GNS cathode. The resolution of the image obtained using the TE cathode was smeared because of its large source size. The brightness $B$ was calculated as

$$B = \frac{I}{dSd\Omega} = \frac{I}{\pi r^2 \pi \alpha^2} \tag{18}$$

where $I$ is the probe current, $dS$ is the source size, $d\Omega$ is the solid angle, $r$ is the radius of the beam, and $\alpha$ is the open angle of the electron optics. For the TE cathode, the beam diameter $2r$ was estimated at about 4 μm and the measured $I$ was about 0.6 μA. Therefore, the brightness $B$ of the TE cathode was estimated to be about $2\times10^8$ $Am^{-2}sr^{-1}$, which coincides with the brightness reported for a tungsten filament TE cathode (Joy et al., 1986). This $B$ value of the TE cathode shows that this method is appropriate for estimating $B$.
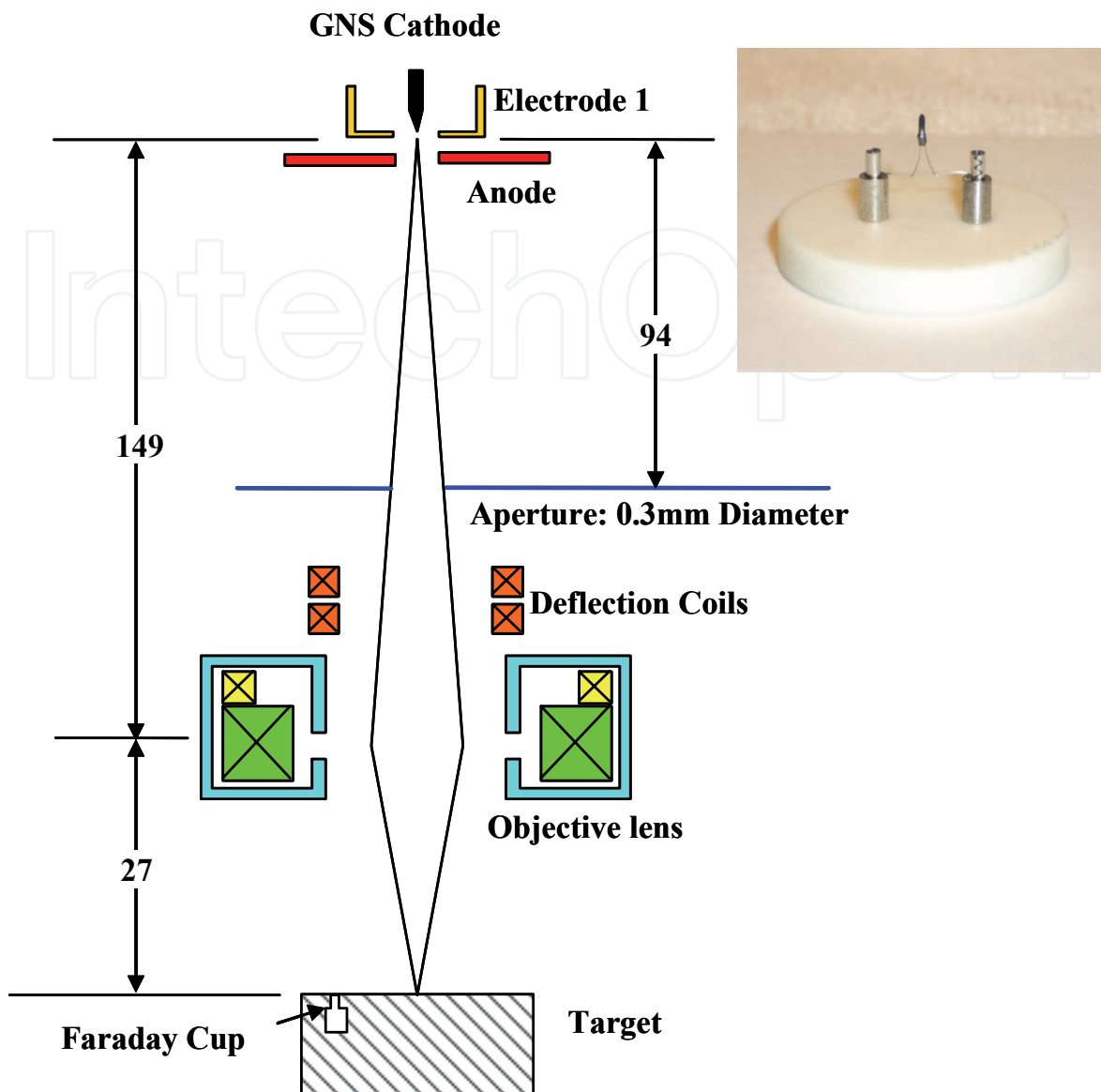
Fig. 20. FE-SEM system equipped with a GNS cathode. (Reprinted with permission, Matsumoto et al. 2007, American Institute of Physics.)

Figure 21 (b) shows the SEM image of the copper mesh obtained using the GNS cathode. The spatial resolution was clearly improved compared to that obtained using the tungsten filament TE cathode. This result shows that an SEM image was obtained using the GNS cathode despite a high residual pressure on the order of $10^{-4}$ Pa. However, as shown in Fig. 21 (b), many horizontal noise lines were observed. This is because the electron beam fluctuation occurred during the scanning of the electron beam to obtain SEM images, which is due to ion bombardment and/or atom adsorption as was described in section 4.

The fluctuation of the emission current originates from the adsorption and desorption of atoms and/or molecules onto emission sites of GNS cathode. To stabilize the emission current, generally, an evacuation of the residual gas to the degree of ultrahigh vacuum ($10^{-9}$ Pa) is performed, and this can be achieved with a massive and costly vacuum system. On the other hand, in section 4, we showed that the number of adsorbed atoms per unit time depends on the temperature of the cathode. Next, we show the reduction of the current

fluctuation by heating the GNS cathode, and show clearer FE-SEM images compared to those obtained with the FE-SEM without heating of GNS cathode at a residual pressure above $10^{-3}$ Pa.

FE-SEM optical system equipped with a GNS-gun designed is the same as described in Fig. 20, where the GNS cathode was attached on the W-filament by using a graphite dispersion in order to heat the cathode, where the temperature of the GNS cathode was measured by a piro- or a radiation-thermometer.

Figure 22 (a) shows FE-SEM images obtained using the GNS cathode at 1200 K. The stability of the emission current was improved compared to that of the GNS cathode without heating, thus leading to acquire clearer images compared to those obtained using the GNS cathode at room temperature. Especially, copper grains are clearly evident, which indicates that the emission source size was reduced compared to TE cathode and that the heated GNS cathode was stable during the acquisition of SEM image (60 s). Figure 22 (b) shows the highest resolution image obtained by using the GNS cathode. Based on this result, the maximum spatial resolution of this SEM optical system was analyzed by the distance between Cu grains, and it was estimated to be 30 nm, which is indicated by the solid white lines shown in Fig. 22 (b). Both the stability and the spatial resolution obtained by the GNS cathode are promising to construct a compact and high resolution FE-SEM system, because it is possible to obtain higher resolution images less than 1 nm by using a commonly used 200-power magnification lens at this high residual pressure region.

The source size was estimated to be 160 nm. The maximum emission current measured by the Faraday cup was about 70 nA. Based on these experimentally determined parameters, the brightness of the GNS cathode was estimated as $5 \times 10^{11}$ Asr$^{-1}$m$^{-2}$, which is similar to that of CNTs (de Jonge et al., 2002). A higher brightness of the order of $10^{13}$ Asr$^{-1}$m$^{-2}$ should be attainable if we apply higher extraction voltage to the cathode.
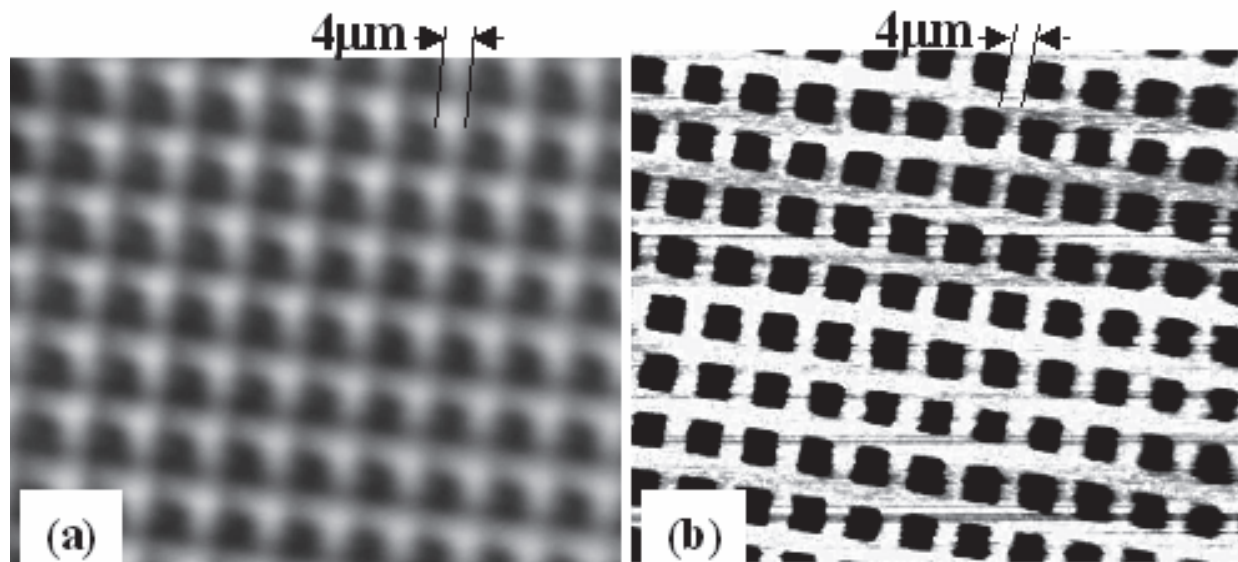


Fig. 21. SEM images of a copper mesh obtained using a (a) TE cathode and (b) GNS cathode. (Reprinted with permission, Neo et al. 2006, American Institute of Physics.)

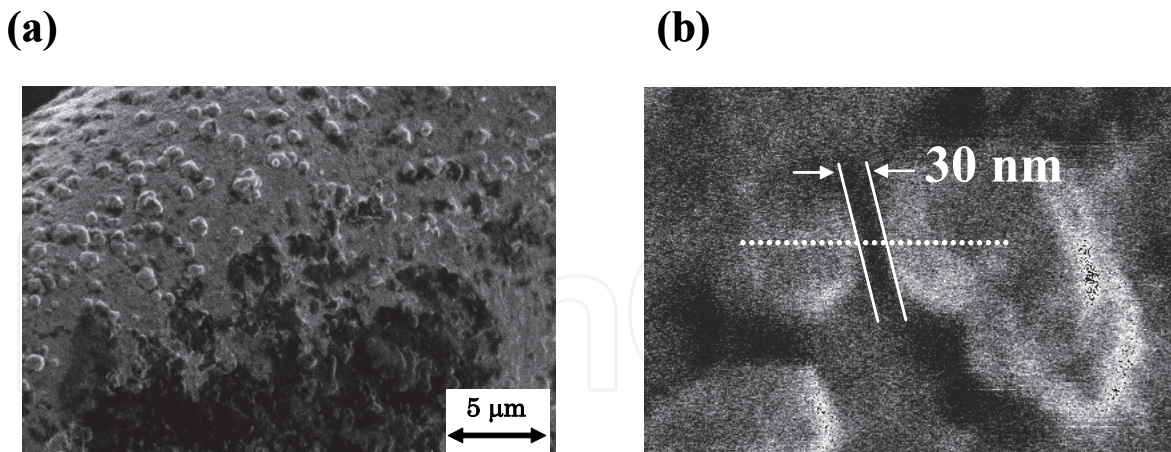**(a)**                                              **(b)**



Fig. 22. (a) Copper mesh images obtained using the GNS cathode. (b) Highest resolution image obtained by using the GNS cathode. (Reprinted with permission, Matsumoto et al. 2007, American Institute of Physics.)

## 7. Conclusion

We showed novel properties of field emission from graphene nanosheets and found that the 2D graphene sheet structure is promising for field emission of electrons owing to the exceptionally large values of carrier mobility and small values of electron mass. From the point of view of emission physics, the macroscale statistical analysis by using the birth and death model gave the insight for the microscale emission mechanism. By proceeding into the atomic level analysis using FEM and FIM, we clarified the emission mechanism both of graphene sheets and of organic materials, where π electron plays an important role for the emission. This new finding not only gives us the solution of the mystery of symmetrical emission patterns discussed for more than 60 years but also paves a way toward a new coherent source of electrons.

After the clarification of the fundamental aspects of GNS, we overviewed the application aspects of the GNS field emitter. The recent progress in the miniature sized x-ray tube clearly shows that GNS is best suited for field emitters. We believe electron emission from graphene will open a new world for classical electron vacuum devices.

## 8. References

Andzelm, J; Govind, N. & Maiti, A. (2006). Nanotube-based gas sensors-role of structure defects. *Chemical Physics Letters*, Vol. 421, pp. 58-62.

Ashworth, F. (1951). Field emission microscopy. *Advances in Electronics*, Vol. 3, pp. 1-42.

Becker, J. (1955). Adsorption on metal surfaces and its bearing on catalysis. *Advances in catalysis*, Vol. 7, pp. 135-211.

Born, M. & Wolf, E. (1999). *Principles of optics; electromagnetic theory of propergation, interference and diffraction of light*. Cambridge University Press. Seventh Edition.

Cowley, J. (1995). *Diffraction Physics*. North-Holland Personal Library, Third Revised Edition.

Dean, K.; Chalamala, B. & Coll, B. et al. (2002). Carbon nanotube field emission electron sources. *New Diamond and Frontier Carbon Technology*, Vol. 12, pp. 165-180.

Dyke, W. & Dolan, W. (1956). Field emission. *Advances in electronics and electron physics*, Vol. 8, pp. 89-185.

Feller, W. (1957). *An introduction to probability theory and its applications*. John Wiley & Sons, New York, Vol. 1, pp. 444-482.

Forbes, R. (2001). Low macroscopic-field electron emission from carbon films and other electrically nanostructured heterogeneous materials: hypotheses about emission mechanism. *Solid State Electronics*, Vol. 45, 779-808.

Fowler, R. & Nordheim, L. (1928). Electron emission in intense electric fields. *Proceedings of the Royal Society (London) A*, Vol. 119, pp. 173-181.

Gadzuk, J. & Plummer, E. (1973). Field emission energy distribution. *Review of modern physics*, Vol. 45, pp. 487-548.

Geim, A. & Novoselov, S. (2007). The rise of graphene. *Nature Material*, Vol. 6, pp. 183-191.

Grujicis, M.; Cao, G. & Singh, R. (2003). The effect of topological defects and oxygen adsorption on the electronic transport properties of single-walled carbon-nanotubes. *Applied Surface Science*, Vol. 211, pp. 166-183.

He, J.; Cutler, P. & Minkovsky, N. (1991). Generalization of Fowler-Nordheim field emission theory for nonplanar metal emitters. *Applied Physics Letters*, Vol. 59, pp. 1644-1646.

Hosoki, S.; Yamamoto, S. & Futamoto, M. et al. (1979). Field emission characteristics of carbon tips. *Surface Science*, Vol. 86, pp. 723-733.

Jacobson, N.; Tegner, B. & Schröder, E. et al. (2002). Hydrogen dynamics in magnesium and graphite. *Computational Materials Science*, Vol. 24, pp. 273-277.

Joy, D.; Roming, Jr., A. & Goldstein, J. (1986). *Principles of analytical electron microscopy*. First Edition, Plenum Press, New York.

Jyouzuka, A.; Nakamura, T. & Onizuka Y. et al. (2010). Emission characteristics and application of graphite nanospine cathode. *The Journal Vacuum Science & Technology B*, Vol. 28, pp. C2C31-C2C34.

Kong, J.; Franklin, N. & Zhou, C. et al. (2000). Nanotube molecular wires as chemical sensors. *Science*, Vol. 287, pp. 622-625.

Liang, S. & Chen, L. (2008). Generalized Fowler-Nordheim theory of field emission of carbon nanotubes. *Physical Review Letters*, Vol. 101, 027602-1-027602-3.

Matsumoto, T. & Mimura, H. (2004). Intense electron emission from graphite nanocraters and their application to time-resolved x-ray radiography. *Applied Physics Letters*, Vol. 84, pp. 1804-1806.

Matsumoto, T. & Mimura, H. (2005). High intensity pulse x-ray generation by using graphite-nanocrater cold cathode. *The Journal Vacuum Science & Technology B*, Vol. 23, pp. 831-835.

Matsumoto, T.; Neo, Y. & Mimura, H. et al. (2007). Stabilization of electron emission from nanoneedles with two dimensional graphene sheet structure in a high residual pressure region. *Applied Physics Letters*, Vol. 90, pp. 103516-1-103516-3.

Matsumoto, T.; Neo, Y. & Mimura, H. et al. (2008). Determining the physisorption energies of molecules on graphene nanostructures by measuring the stochastic emission-current fluctuation. *Physical Review E*, Vol. 77, pp. 031611-1-031611-4.

Murr, L. & Inal, O. (1971). Field ion microscopy of graphite fibers. *Journal of Applied Physics*, Vol. 42, pp. 3487-3493.

Müller, E. (1953). Feldemission. *Ergebnisse d. Exakt Naturwiss*, Vol. XXVII, pp. 290-360.

Neo, Y; Matsumoto, T. & Tomita, M. et al. (2010). Revealing real images of cloverleaf pattern emission sites by using field ion microscopy. *The Journal Vacuum Science & Technology B*, Vol. 28, pp. C2A1-C2A4.

Neo,Y.; Mimura, H. & Matsumoto, T. (2006). Field emision characteristics of a graphite nanoneedle cathode and its application to scanning electron microscopy. *Applied Physics Letters*. Vol. 88, pp. 073511-1-073511-3.

Novoselov, S.; Geim, A., & Morozov, S., et al. (2005). Two-dimensional gas of massless Dirac fermions in graphene. *Nature*, Vol. 438, pp. 197-200.

Tran, F.; Weber, J. & Wesolowski, T. et al. (2002). Physisorption of molecular hydrogen on polycyclic aromatic hydrocarbons: A theoretical study. *The Journal of Physical Chemistry B*. Vol. 106, pp. 8689-8696.

Ulbricht, H.; Gunnar, M. & Hertel, T. (2002). Physisorption of molecular oxygen on single-wall carbon nanotube bundles and graphite. *Physical Review B*, Vol. 66, pp. 075404-1-075404-7.

Ulbricht, H.; Zacharia, R. & Cindir, N. et al. (2006). Thermal desorption of gases and solvents from graphite and carbon nanotube surfaces. *Carbon*, Vol. 44, pp. 2931-2942.

Vidali, G.; Ihm, G. & Kim, H. et al. (1991). Potentials of physical adsorption. *Surface Science Reports*, Vol. 12, pp. 133-181.

Williams, W. (1968). Field ion-microscopy of graphite. *Journal of Applied Physics*, Vol. 39, pp. 2131-2132.

Wolf, P. (1954). Die abbildung molekularer objekte mit dem Feldelektronenmikroskop. *Zeitshrift für angewandte physik*, Vol. 12, pp529-535.

Ximen, J. (1994). Fundamentals of electron optics. *Advances in Optical and electron microscopy*. Vol. 13, pp. 243-301.

Yamamoto, S.; Hosoki, S. & Fukuhara, S. et al. (1979). Stability of carbon field emission current. *Surface Science*, Vol. 86, pp. 734-742.

Zhang, Y.; Tan, Y. & Stormer, H. et al. (2005). Experimental observation of the quantum hall effect and Berry's phase in graphene. *Nature*, Vol. 438, pp. 201-204.

Zhao, J.; Buldum, A. & Han, J. et al. (2002). Gas molecule adsorption in carbon nanotubes and nanotube bundles. *Nanotechnology*, Vol. 13, pp. 195-200.

de Jonge, N.; Lamy, Y. & Schoots, K. et al. (2002). High brightness electron beam from a muti-walled carbon nanotube. *Nature*, Vol. 420, pp. 393-395.
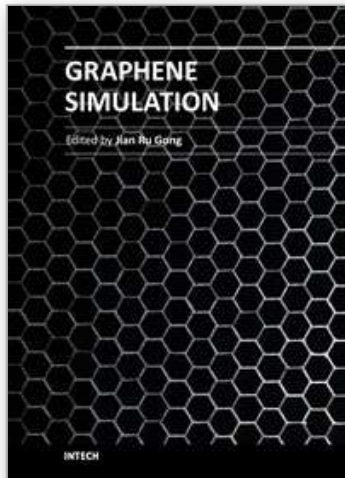
**Graphene Simulation**

Edited by Prof. Jian Gong

Graphene, a conceptually new class of materials in condensed-matter physics, has been the interest of many theoretical studies due to the extraordinary thermal, mechanical and electrical properties for a long time. This book is a collection of the recent theoretical work on graphene from many experts, and will help readers to have a thorough and deep understanding in this fast developing field.

**How to reference**

In order to correctly reference this scholarly work, feel free to copy and paste the following:

Takahiro Matsumoto, Tomonori Nakamura, Yoichiro Neo, Hidenori Mimura and Makoto Tomita (2011). Field Emission from Graphene Nanosheets, Graphene Simulation, Prof. Jian Gong (Ed.), ISBN: 978-953-307-556-3, InTech, Available from: http://www.intechopen.com/books/graphene-simulation/field-emission-from-graphene-nanosheets

# INTECH
open science | open minds